

Search for supersymmetry in diphoton final states with the CMS detector

Matthew Lawrence Joyce

April 1, 2021

CONTENTS

| | | |
|-------|----------------------------------|----|
| 1. | <i>The Standard Model</i> | 7 |
| 2. | <i>Supersymmetry</i> | 8 |
| 3. | <i>The Large Hadron Collider</i> | 9 |
| 3.1 | Introduction | 9 |
| 3.2 | Injection Complex | 9 |
| 3.3 | Tunnel and Magnets | 10 |
| 3.4 | Luminosity | 12 |
| 4. | <i>Compact Muon Solenoid</i> | 14 |
| 4.1 | Introduction | 14 |
| 4.2 | Coordinate System | 15 |
| 4.3 | Tracker | 16 |
| 4.3.1 | Pixel Detector | 16 |
| 4.3.2 | Strip Detector | 17 |
| 4.4 | Electromagnetic Calorimeter | 18 |
| 4.4.1 | Crystals | 19 |
| 4.4.2 | Barrel and Endcaps | 19 |
| 4.4.3 | Preshower layer | 21 |
| 4.4.4 | Performance | 21 |
| 4.5 | Hadronic Calorimeter | 22 |
| 4.6 | Superconducting Solenoid | 23 |
| 4.7 | Muon System | 23 |
| 5. | <i>MIP Timing Detector (MTD)</i> | 26 |
| 5.1 | Introduction | 26 |
| 5.2 | Barrel Timing Layer | 27 |
| 6. | <i>CMS Trigger System</i> | 29 |
| 6.1 | L1 trigger | 29 |
| 6.1.1 | Calorimeter trigger | 29 |

| | | |
|-------|--|----|
| 6.1.2 | Muon trigger | 30 |
| 6.1.3 | Global Trigger | 31 |
| 6.2 | High Level Trigger | 31 |
| 6.3 | Trigger efficiency | 31 |
| 7. | <i>CMS Particle and Event Reconstruction</i> | 32 |
| 7.1 | Tracks | 32 |
| 7.2 | Calorimeter clusters | 33 |
| 7.3 | Object identification | 33 |
| 7.3.1 | Muons | 33 |
| 7.3.2 | Electrons | 34 |
| 7.3.3 | Photons | 35 |
| 7.3.4 | Jets | 36 |
| 7.4 | Missing transverse momentum | 36 |
| 8. | <i>Data Analysis</i> | 37 |
| 8.1 | Overview | 37 |
| 8.2 | Data | 37 |
| 8.3 | Monte Carlo samples | 38 |
| 8.4 | Object definitions | 38 |
| 8.4.1 | Photons | 39 |
| 8.4.2 | Electrons | 40 |
| 8.4.3 | Muons | 40 |
| 8.5 | Backgrounds | 40 |
| 8.5.1 | Instrumental background | 40 |
| 8.5.2 | Electroweak background | 41 |
| 8.5.3 | Irreducible background | 42 |

LIST OF FIGURES

| | | |
|-----|--|----|
| 3.1 | LHC interaction points | 10 |
| 3.2 | Layout of LHC accelerator complex [16]. | 11 |
| 3.3 | Proton bunch capture onto RF bucket [6]. | 12 |
| 3.4 | Cross section of LHC dipole [9] | 13 |
| 3.5 | Integrated luminosity delivered by the LHC to the CMS experiment each year from 2010-2018. | 13 |
| 4.1 | Schematic of CMS detector [19] | 14 |
| 4.2 | Transverse slice of the CMS detector[7]. | 15 |
| 4.3 | Cross section (side) of CMS tracker prior to the Phase 1 upgrade during the year-end technical stop of 2016/2017. Each line represents a detector module while double lines indicate back-to-back strip modules. Surrounding the pixel tracker (PIXEL) is the strip detector, which is divided into the Tracker Inner Barrel (TIB), Tracker Outer Barrel (TOB), Tracker Inner Disks (TID), and Tracker Endcaps (TEC). Reprinted from Reference [12]. | 17 |
| 4.4 | Cross section (side) of pixel detector. The lower half , labeled "Current", shows the design prior to 2017 while the upper half, labeled "Upgrade", shows the design after the upgrade. Reprinted from Resource [11] | 18 |
| 4.5 | PbWO ₄ crystals. Left: EB crystal with APD. Right: EE crystal with VPT. Reprinted from [13] | 20 |
| 4.6 | Schematic of ECAL. Reprint from [13] | 21 |
| 4.7 | Longitudinal view of HCAL [2] | 23 |
| 4.8 | Longitudinal slice of CMS detector while operating at 3.8-T central magnetic field. The right-hand side of the figure shows a mapping of the magnetic field lines while the left-hand side shows a mapping of the field strength. Reprint from [10] . . . | 24 |

| | | |
|-----|---|----|
| 4.9 | Cross-section of one quadrant of the CMS detector. The DTs are labeled as "MB" (Muon Barrel) and the CSCs are labelled as "ME" (Muon Endcap). The RPCs are "RB" for those in the barrel and "RE" for those in the endcap. Reprint from [20]. | 25 |
| 5.1 | Timeline for LHC | 26 |
| 5.2 | Vertices from a simulated 200 pileup event. Need to replace this with the figure from the TDR. | 27 |
| 6.1 | L1 trigger system. Reprint from [3] | 30 |
| 7.1 | The Bremsstrahlung photons continue along a straight trajectory while the electron path is bent by the magnetic field. This results in energy deposited in the calorimeter for such electrons to be spread out along the ϕ -direction. | 35 |
| 8.1 | Two examples of GGM supersymmetry breaking processes resulting in final states containing two photons and missing transverse momentum. The T5gg model (left) shows gluinos produced from $p - p$ collisions which subsequently result in two neutralinos, each decaying to a photon and a gravitino. The T6gg model (right) shows squarks produced from $p - p$ collisions following a similar decay chain. | 37 |
| 8.2 | Mismeasurement of Jet3 results in an imbalance in the events transverse momentum. | 41 |

LIST OF TABLES

| | | |
|-----|---|----|
| 4.1 | Summary of signals expected for each particle type in each sub-detector. | 15 |
| 6.1 | Primary HLT | 31 |
| 8.1 | Data Samples | 38 |
| 8.2 | Summary of loose ID photons cuts | 39 |

1. THE STANDARD MODEL

2. SUPERSYMMETRY

3 3. THE LARGE HADRON COLLIDER

4 3.1 *Introduction*

5 The Large Hadron Collider (LHC) is a 26.7 kilometer-long, two-ring particle
6 accelerator and collider located on the border of France and Switzerland at
7 the European Organization for Nuclear Research (CERN). During normal
8 operations the LHC maintains two counter-rotating beams of proton bunches
9 that collide at four interaction points (IP) with up to $\sqrt{s} = 14$ TeV center
10 of mass energy and a luminosity of $10^{34}\text{cm}^{-2}\text{s}^{-1}$. The ALICE (Point 2),
11 ATLAS (Point 1), CMS (Point 5), and LHC-b experiments each have a
12 detector at one of these interaction points as scene in Figure 3.1 . The CMS
13 and ATLAS are general-purpose detectors while LHC-b specializes in beauty
14 quark studies. ALICE is a heavy-ion experiment which uses $^{208}\text{Pb} - p$ or
15 $^{208}\text{Pb} - ^{208}\text{Pb}$ collisions that can also be produced by the LHC.

16 3.2 *Injection Complex*

17 In order to bring the protons from rest up to their target collision energy
18 a series of accelerators, as shown in Figure 3.2, are used. The acceleration
19 sequence begins with the injection of hydrogen gas into a duoplasmatron.
20 Here a bombardment of electrons ionize the hydrogen atoms while an electric
21 field pushes them through the duoplasmatron cavity. The result is 100 keV
22 protons being passed on to a quadrupole magnet which guides them into
23 the aperture of a linear accelerator (LINAC2). The radio frequency (RF)
24 cavities in LINAC2 accelerate the protons up to 50 MeV. At this point the
25 protons are sent into one of four rings in the Proton Synchrotron Booster
26 (PSB). The PSB repeatedly accelerates the protons around a circular path
27 until they reach an energy of 1.4 GeV. The bunches of protons from each PSB
28 ring are then sequentially injected into the single-ringed Proton Synchrotron
29 (PS). Each bunch injected into the PS are captured by one of the "buckets"
30 (Figure 3.3) provided by the PS RF system which also manipulates the
31 bunches into the desired profile and proton density. These proton bunches
32 are accelerated to 25 GeV and injected into the Super Proton Synchrotron

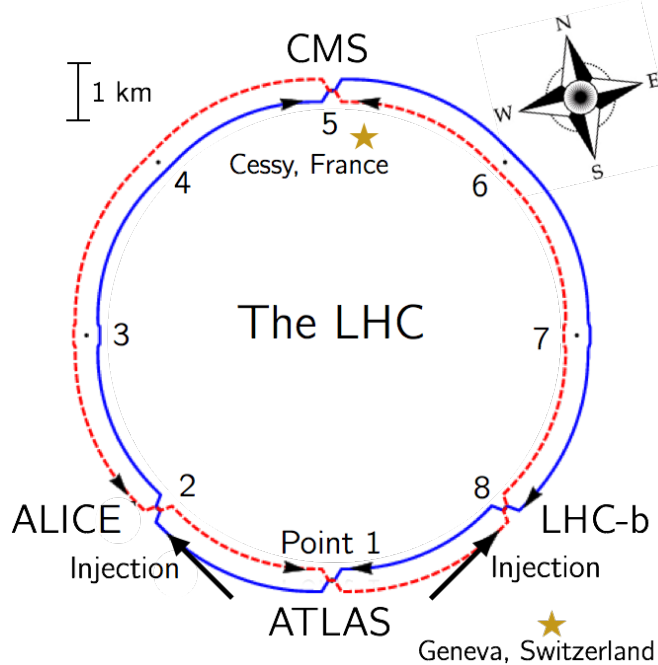


Fig. 3.1: Interaction points of the LHC

³³ (SPS) where they are accelerated to 450 GeV. Finally the proton bunches
³⁴ are injected into the LHC ring where they are accelerated to 6.5 TeV and
³⁵ collided in 25 ns intervals to yield a center of mass energy of $\sqrt{s} = 13$ TeV.

³⁶ 3.3 Tunnel and Magnets

³⁷ The LHC was designed to produce collisions with up to $\sqrt{s} = 14$ TeV. That
³⁸ requires confining and guiding 7 TeV protons around the circumference of
³⁹ the LHC ring. The ring is housed in a 4 meter-wide underground tunnel
⁴⁰ that ranges in depth between 45 and 170 meters below the surface. This
⁴¹ tunnel was repurposed from the Large Electron-Positron (LEP) Collider
⁴² which previously occupied the space. For this reason the tunnel is not
⁴³ completely circular but is instead made up of alternating curved and straight
⁴⁴ sections of 2500 m and 530 m in length respectively. The straight sections,
⁴⁵ labeled 1-8 in Figure 3.1, are used as either experimental facilities or sites for
⁴⁶ hardware necessary for LHC operations such as RF cavities for momentum
⁴⁷ cleaning, quadrupole magnets for beam focusing, and sextupole magnets for
⁴⁸ acceleration and betatron cleaning.

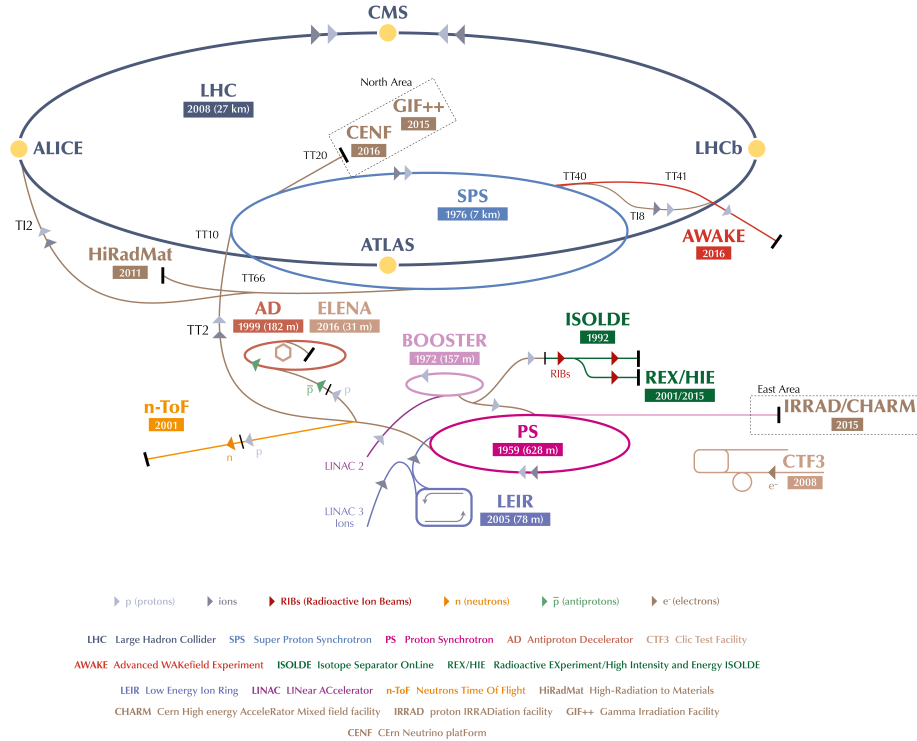


Fig. 3.2: Layout of LHC accelerator complex [16].

49 Steering a 7 TeV proton beam around the curved sections requires a mag-
 50 netic field of 8.33 Tesla which is provided by 1223 superconducting dipole
 51 magnets cooled to 1.9 K. A cross section of the LHC dipole is shown in
 52 Figure 3.4. Supercooled liquid helium flows through the heat exchanger
 53 pipe to cool the iron yolk to a temperature of 1.9 K. Ultra high vacuum
 54 is maintained in the outer volume to provide a layer of thermal insulation
 55 between the inner volume and the outer steel casing. Inside the iron yolk is a
 56 twin bore assembly of niobium-titanium superconducting coils. Two parallel
 57 beam pipes are located within the focus of the superconducting coils. This
 58 is the ultra high vacuum region where the subatomic particles are confined
 59 as they travel around the LHC ring.

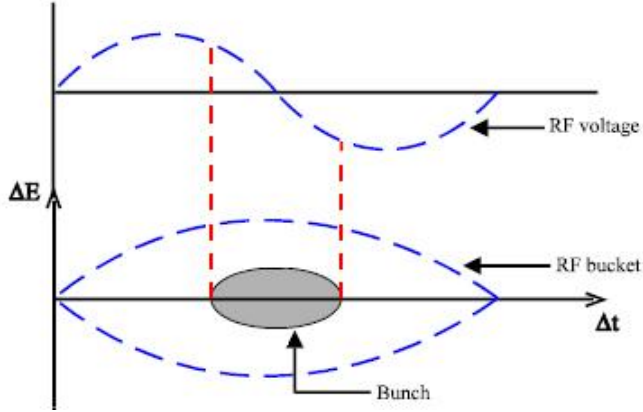


Fig. 3.3: Proton bunch capture onto RF bucket [6].

3.4 Luminosity

61 The number of events generated per second for specific process having cross-
62 section σ_{event} is given by:

$$\frac{dN_{event}}{dt} = L\sigma_{event} \quad (3.1)$$

63 where L is the machine luminosity. The machine luminosity for a Gaussian
64 beam distribution can be written in terms of the beam parameters as:

$$L = \frac{N_b^2 n_b f_{rev} \gamma_r}{4\pi \epsilon_n \beta_*} F \quad (3.2)$$

65 where N_b is particle density in each bunch, n_b is the number of bunches
66 in each beam, f_{rev} is the frequency of revolution, and γ_r is the relativistic
67 gamma factor. The variables ϵ_n and β_* are the normalized transverse beam
68 emittance and the beta function at the IP respectively, while F is the geo-
69 metric reduction factor depending due to the beams' crossing angle at the
70 IP. [16]

71 The total number of events produced over a given amount of time would
72 then be

$$N_{event} = \sigma_{event} \int L dt = \sigma_{event} L_{integrated}. \quad (3.3)$$

73 The integrated luminosity delivered each year to the CMS experiment is
74 shown in 3.5. The analysis presented here uses data collected from the 2016,
75 2017, and 2018 campaigns which gives a combined integrated luminosity of
76 158.7 fb^{-1} .

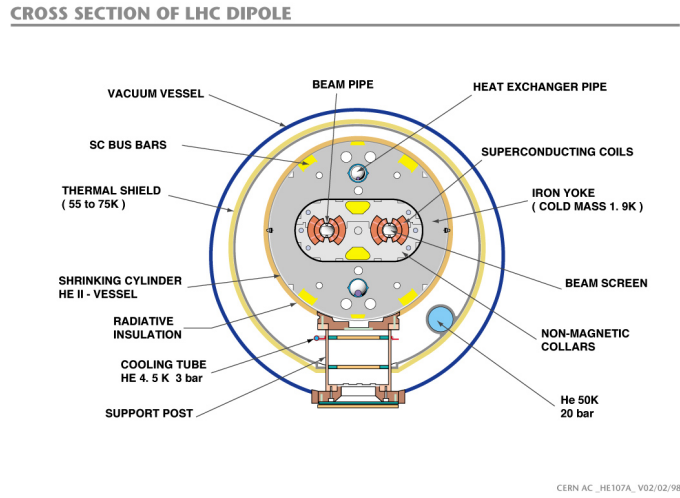


Fig. 3.4: Cross section of LHC dipole [9]

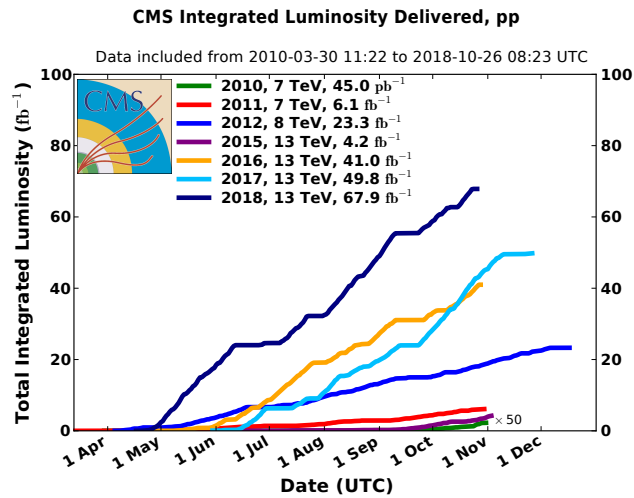


Fig. 3.5: Integrated luminosity delivered by the LHC to the CMS experiment each year from 2010-2018.

4. COMPACT MUON SOLENOID

4.1 Introduction

79 About 100 meters below the town of Cessy, France at Point 5 is the Compact
 80 Muon Solenoid (CMS). The CMS is a general purpose detector weighing
 81 14,000 tonnes with a length of 28.7 meters and a 15.0-meter diameter that
 82 was designed to accurately measure the energy and momentum of particles
 83 produced in the proton-proton or heavy-ion collisions at the LHC [13]. A
 84 perspective view of the detector is shown in Figure 4.1. In order to get
 85 a full picture of what is being produced by the collisions the CMS detector
 86 must be able identify the resulting particles as well as accurately measure
 87 their energy and momentum. For this reason the detector was designed to
 88 be a collection of specialized sub-detectors, each of which contributes data
 used in the reconstruction of a collision.

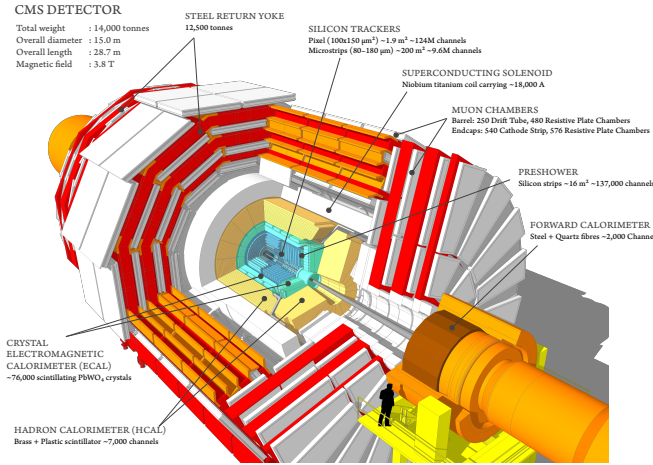


Fig. 4.1: Schematic of CMS detector [19]

90 At the heart of the CMS detector is a 3.8-Tesla magnetic field produced
 91 by a superconducting solenoid. Inside the 6-meter diameter solenoid are

three layers of sub-detectors. These make up the inner detector and are, in order from innermost to outermost, the silicon tracker, the electromagnetic calorimeter (ECAL), and the hadronic calorimeter (HCAL). Outside the solenoid is the muon system. A transverse slice of the detector (Figure 4.2) shows the sub-detectors and how different types of particles interact with them. Table 4.1 shows a summary of which sub-detectors are expected to produce signals for different types of particles.

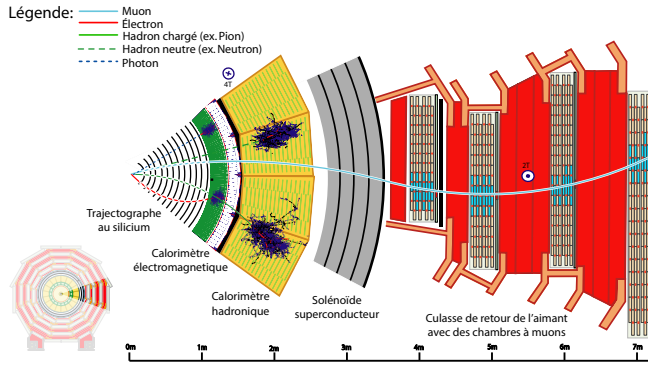


Fig. 4.2: Transverse slice of the CMS detector[7].

| Particle | Tracker | ECAL | HCAL | Muon |
|--------------------------------|---------|------|------|------|
| Photons | No | Yes | No | No |
| Electrons | Yes | Yes | No | No |
| Hadrons (charged) | Yes | Yes | Yes | No |
| Hadrons (neutral) | No | No | Yes | No |
| Muons | Yes | Yes | Yes | Yes |
| Invisible (ν , SUSY, etc) | No | No | No | No |

Tab. 4.1: Summary of signals expected for each particle type in each sub-detector.

4.2 Coordinate System

The origin of the coordinate system used by CMS is centered at the nominal collision point in the center of the detector. A right-handed Cartesian system is used with the x-axis pointing radially inward toward the center of the LHC ring, y-axis pointing vertically upward, and the z-axis pointing tangent to

104 the LHC ring in the counterclockwise direction as viewed from above. CMS
 105 also uses an approximately Lorentz invariant spherical coordinate system
 106 spanned by three basis vectors. They are the transverse momentum p_T ,
 107 pseudorapidity η , and azimuthal angle ϕ . The transverse momentum and
 108 azimuthal angle translate to the Cartesian system in the following ways
 109 using the x and y-components of the linear momentum:

$$p_T = \sqrt{(p_x)^2 + (p_y)^2} \quad (4.1)$$

$$\phi = \tan^{-1} \frac{p_y}{p_x} \quad (4.2)$$

110 while the pseudorapidity can be translated using the polar angle θ relative
 111 the positive z-axis as

$$\eta = -\ln[\tan \frac{\theta}{2}] \quad (4.3)$$

113 4.3 Tracker

114 The innermost sub-detector in CMS is the silicon tracker. The tracker is
 115 used to reconstruct tracks and vertices of charged particles. In order to give
 116 precise reconstruction of charged particle trajectories it needs to be position
 117 as close as possible to the IP and have high granularity. The close proximity
 118 to the IP requires the materials to be tolerant to the high levels of radiation
 119 in that region. Being the innermost sub-detector it must also minimally
 120 disturb particles as they pass through it into the other sub-detectors. These
 121 criteria led to the design of the tracker using silicon semiconductors.

122 The silicon tracker is made up of two subsystems, an inner pixel detector
 123 and an outer strip tracker which are oriented in a cylindrical shape with an
 124 overall diameter of 2.4 m and length of 5.6 m centered on the interaction
 125 point. Both subsystems consist of barrel and endcap regions which can be
 126 seen in Figure 4.3.

127 4.3.1 Pixel Detector

128 The pixel detector is the innermost subsystem in the silicon tracker and
 129 spans the pseudorapidity range $|\eta| < 2.5$ and is responsible for small im-
 130 pact parameter resolution which is important for accurate reconstruction of
 131 secondary vertices [13]. In order to produce these precise measurements a
 132 very high granularity is required. In addition to this the proximity to the
 133 IP means that one expects there to be high occupancy of the tracker. These
 134 constraints are met by using pixels with a cell size of $100 \times 150 \mu\text{m}^2$.

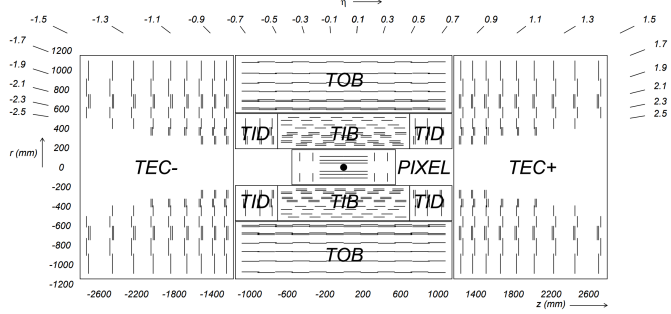


Fig. 4.3: Cross section (side) of CMS tracker prior to the Phase 1 upgrade during the year-end technical stop of 2016/2017. Each line represents a detector module while double lines indicate back-to-back strip modules. Surrounding the pixel tracker (PIXEL) is the strip detector, which is divided into the Tracker Inner Barrel (TIB), Tracker Outer Barrel (TOB), Tracker Inner Disks (TID), and Tracker Endcaps (TEC). Reprinted from Reference [12].

135 The original pixel detector was designed for operation at the nominal
 136 instantaneous luminosity of $10^{34} \text{ cm}^{-2}\text{s}^{-1}$ with 25 ns between proton bunch
 137 crossings, resulting in on average about 25 proton-proton interactions occur-
 138 ring per bunch crossing or pileup [12]. During the LHC technical shutdown
 139 of 2016/17, the pixel detector underwent the scheduled Phase 1 upgrade
 140 which would allow operation at higher levels of instantaneous luminosity
 141 and pileup. Figure 4.4 shows a cross sectional view in the r - z plane. Prior
 142 to 2017 there were three barrel layers and two endcap layers on each side
 143 which provide three very precise space points for each charged particle. The
 144 upgrade decreased the radius of the innermost barrel layer from 4.4 cm to
 145 3.0 cm and added a fourth barrel layer as well as adding third endcap layer
 146 to each side. Each of the endcap layers consisted of two half-disks populated
 147 with pixel modules whereas the upgraded endcap layers were split into inner
 148 and outer rings. [11]

149 4.3.2 Strip Detector

150 The silicon strip detector surrounds the pixel detector and is comprised of
 151 four subsystems, the Tracker Inner Barrel (TIB), the Tracker Outer Barrel
 152 (TOB), the Tracker Inner Disks (TID), and the Tracker Endcaps (TEC),
 153 all of which can be seen in Figure 4.3 [13]. The TIB and TID both use
 154 320 μm thick silicon micro-strip sensors oriented along z and r respectively.
 155 The TIB has four layers while the TID is composed of three layers. This

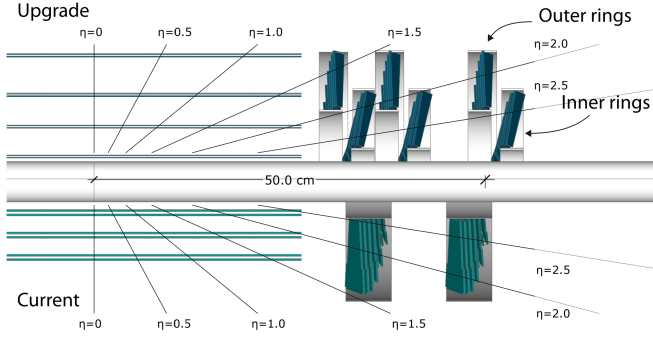


Fig. 4.4: Cross section (side) of pixel detector. The lower half , labeled "Current", shows the design prior to 2017 while the upper half, labeled "Upgrade", shows the design after the upgrade. Reprinted from Resource [11]

geometry allows the TIB and TID to combine to provide up to four $r - \phi$ measurements on charged particle trajectories.

Surrounding the TIB and TID is the TOB, which extends between $z \pm 118$ cm. This subsystem consists of six layers of 500 μm thick silicon micro-strip sensors with strip pitches ranging from 122 μm to 183 μm , providing six more $r - \phi$ measurements in addition to those from the TIB/TID subsystems. Beyond the z range of the TOB is the TEC. Each TEC is made up of nine disks. Each of the nine disks has up to seven concentric rings of micro-strip sensors oriented in radial strips with those on the inner four rings being 320 μm thick and the rest being 500 μm thick, providing up to nine ϕ measurements for the trajectory of a charged particle.

To provide additional measurements of the z coordinate in the barrel and r coordinate in the disks a second micro-strip detector module is mounted back-to-back with stereo angle 100 mrad in the first two layers of the TIB and TOB, the first two rings of the TID, and rings 1, 2, and 5 of the TEC. The resulting single point resolution is 230 μm in the TIB and 530 μm in the TOB. The layout of these subsystems ensures at least nine hits for $|\eta| < 2.4$ with at least four of hits yielding a 2D measurement.

4.4 Electromagnetic Calorimeter

The electromagnetic calorimeter (ECAL) lies just outside the tracker and is a hermetic homogeneous calorimeter designed to measure the energy deposited by electrons and photons. It consists of a central barrel (EB) with 61200 lead tungstate (PbWO_4) crystals which is closed by two endcaps (EE), each

179 having 7324 crystals. Highly-relativistic charged particles passing through a
180 crystal primarily lose energy by producing bremsstrahlung photons. Photons
181 lose energy by producing $e^- - e^+$ pairs. In front of each EE is a preshower
182 (ES) detector which acts as a two-layered sampling calorimeter. The crystals
183 in the EB are instrumented with avalanche photodiodes (APDs) while the
184 EE crystals are instrumented with vacuum phototriodes (VPTs). The ECAL
185 design was strongly driven to be sensitive to the di-photon decay channel
186 of the Higgs boson. This led to the design of a calorimeter that was fast,
187 radiation-hard, and had good spatial and energy resolution.

188 4.4.1 Crystals

189 In order to provide a good spacial resolution it was necessary for the ECAL
190 to have a fine granularity. The small Molier radius (22 mm) and short radia-
191 tion length (8.9 mm) of PbWO₄ allows for fine granularity while maintaining
192 good energy resolution by containing nearly all of the energy from an EM
193 shower without the need for a restrictively thick crystal layer. The PbWO₄
194 scintillation is also fast enough that approximately 80 percent of an EM
195 shower is produced within 25 ns, which is the also the amount of time be-
196 tween bunch crossings at the LHC. These crystals have a Gaussian-shaped
197 spectrum spanning from 360 nm to 570 nm with a maximum at approx-
198 imately 440 nm. While PbWO₄ is relatively radiation-hard, the amount
199 of ionizing radiation seen by the crystal leading up to the HL-LHC era of
200 operations causes wavelength-dependent degradation in light transmission.
201 The scintillation mechanism however is unchanged so this damage can be
202 tracked and accounted for by injecting laser light near the peak wavelength
203 of the emission spectrum into the crystals to monitor optical transparency.

204 Light produced in the crystal is transmitted along its length and col-
205 lected at the rear by either an APD in the EB or a VPT in one of the EE.
206 Light output is temperature dependent so the crystals are kept at precisely
207 18°C at which the yield is about 4.5 photoelectrons per MeV. The EB and
208 EB crystals, which have a tuncated pyramidal shape to match the lateral de-
209 velopment of the shower, along with their photosensors are shown in Figure
210 4.5.

211 4.4.2 Barrel and Endcaps

212 The EB covers the pseudorapidity range $|\eta| < 1.479$ and uses crystals that
213 are 230 mm long, which corresponds to 25.8 radiation lengths. The front
214 face of each crystal measures 22×22 mm² while the rear face measures 26×26

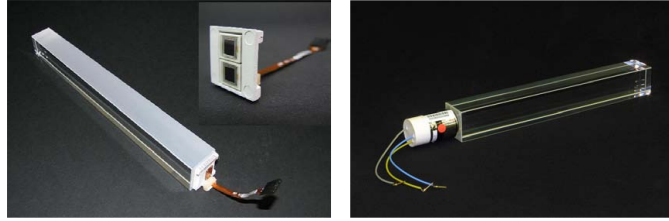


Fig. 4.5: PbWO₄ crystals. Left: EB crystal with APD. Right: EE crystal with VPT. Reprinted from [13]

mm². These are grouped in 36 supermodules (SM), each comprised of 1700 crystals arranged in a 20×85 grid in $\phi \times \eta$. Each SM spans half the length of the barrel and covers 20° in ϕ . On the back face of each crystal is a pair of APDs (semiconductor diodes). APDs are compact, immune to the longitudinal 3.8 T magnetic field produced by the solenoid at this location, and resistant to the radiation levels expected in the EB over a ten year period. They also have high enough gain to counter to low light yield of the crystals. All of this makes them an ideal choice for use in the EB. Each APD has an active area of 5 × 5 mm² and are operated at a gain of 50 which requires a bias voltage between 340 and 430 V. As the gain of the APDs is highly dependent on the applied bias voltage and any gain instability would translate to degradation in energy resolution, very stable power supplies are used to maintain voltages within a few tens of mV.

The EE cover the pseudorapidity range 1.497 < | η | < 3.0. The crystals in the EE have a 28.62×28.62 mm² front face cross section and 30×30 mm² rear face cross section. Each crystal is 220 mm long which corresponds to 24.7 radiation lengths and are grouped in 5×5 units called supercrystals (SCs). Two halves, called *Dees*, make up each EE. Each Dee contains 138 SCs and 18 partial SCs which lie along the inner and outer circumference. On the back of each crystal in EE is a VPT which is a conventional photomultiplier with a single gain stage. While not as compact as the APDs used in the EB, the VPTs are a more suitable for the more hostile environment at higher η . Each VPT has a 25-mm diameter and approximately 280 mm² of active area. Though the VPT gain and quantum efficiency are lower than that of the APDs this is offset by the larger active area allowing for better light collection. Figure 4.6 shows the orientation of the crystals, modules, and supermodules within the ECAL. [13]

242

4.4.3 Preshower layer

243 In front of each EE is a preshower (ES) detector. The main purpose of the
 244 ES is to identify photons resulting from $\pi^0 \rightarrow \gamma\gamma$ within the pseudorapidity
 245 range $1.653 < |\eta| < 2.6$, but it also aids in the identification of electrons
 246 against minimum ionizing particles (MIPs) and provides a spacial resolution
 247 of 2 mm compared to the 3 mm resolution of the EB and EE. The ES acts
 248 as a two-layered sampling calorimeter. Lead radiators make up the first
 249 layer. These initiate electromagnetic showers from incoming electrons or
 250 photons. The deposited energy and transverse profiles of these showers are
 251 then measured by the silicon strip sensors which make up the second layer.

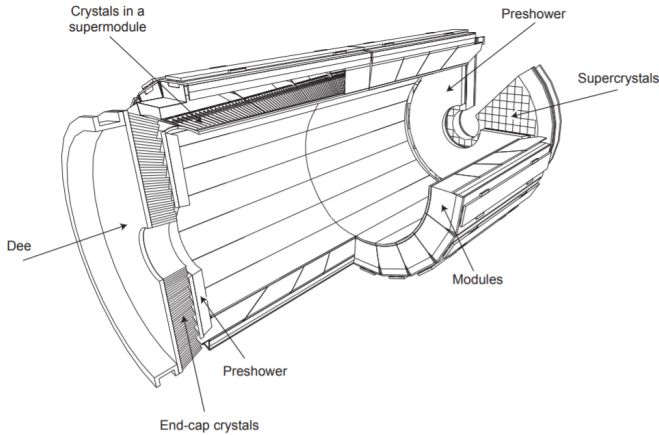


Fig. 4.6: Schematic of ECAL. Reprint from [13]

252

4.4.4 Performance

253 The energy resolution of the ECAL can be parameterized as

$$\frac{\sigma}{E} = \frac{S}{\sqrt{E}} \oplus \frac{N}{E} \oplus C \quad (4.4)$$

254 where S is the stochastic term characterizing the size of photostatistical
 255 fluctuations, N is the term characterizing the contributions of electronic,
 256 digital, and pileup noise, and C is a constant which accounts for crystal
 257 performance non-uniformity, intercalibration errors, and leakage of energy
 258 from the back of a crystal. The values for these terms, as measured in a
 259 beam test using 20 to 250 GeV electrons, are $S = 0.028 \text{ GeV}^{1/2}$, $N = 0.12$
 260 GeV, and $C = 0.003$. [13]

 261 4.5 Hadronic Calorimeter

262 In the space between the bore of the superconducting magnet and the ECAL
 263 is the Hadronic Calorimeter (HCAL) [2]. The HCAL is a sampling calorime-
 264 ter used for the measurement of hadronic jets and apparent missing trans-
 265 verse energy resulting from neutrinos or exotic particles. It is made up of al-
 266 ternating layers of plastic scintillator tiles and brass absorbers. EM showers
 267 are generated by charged/neutral hadrons in the brass absorber. Charged
 268 particles in the shower then produce scintillation light in the plastic scintil-
 269 lator. Wavelength-shifting optical fibers embedded in the scintillator collect
 270 and guide the scintillation light to pixelated hybrid photodiodes. A longi-
 271 tudinal cross-section view in Figure 4.7 shows the geometric layout of the
 272 HCAL’s barrel (HB), outer barrel (HO), endcap (HE), and forward (HF)
 273 sections. The HB is comprised of 17 scintillator layers extending from 1.77
 274 to 1.95 m and covers the pseudorapidity range of $|\eta| < 1.4$. The HO lies
 275 outside the solenoid and is composed of only scintillating material. This
 276 increases the interaction depth of the calorimeter system to a minimum of
 277 $11\lambda_I$ for $|\eta| < 1.26$ and thus reduces energy leakage. Also located inside
 278 the solenoid are the two HE which cover pseudorapidities $1.3 < |\eta| < 3.0$
 279 and provide a thickness of $10\lambda_I$. In the forward region is the HF. This is
 280 located 11.2 m away from the IP and covers the $2.9 < |\eta| < 5.2$. As the
 281 HF is exposed to the highest levels of particle flux, it uses quartz fibers em-
 282 bedded in steel absorbers rather than the materials used in the other parts
 283 of the HCAL. Showers initiated by the absorbers produce Cerenkov light
 284 in the quartz which transmits along to the fibers to photomultiplier tubes
 285 (PMTs).

286 The HCAL inherently has lower energy resolution than the ECAL. A
 287 large portion of the energy from hadronic showers is deposited in the ab-
 288 sorbers and never makes it to the scintillation material. There are also
 289 the possibilities that showers can be initiated prior to the particles reach-
 290 ing HCAL or a charged particle could deposit energy in the ECAL through
 291 bremsstrahlung. The combined energy resolution of the ECAL and the
 292 HCAL barrels can be parameterized as

$$\frac{\sigma}{E} = \frac{S}{\sqrt{E}} \oplus C, \quad (4.5)$$

293 where E is the energy of the incident particle. These quantities were mea-
 294 sured in a beam test using 2 to 350 GeV/c hadrons, electrons, and muons.
 295 The stochastic term is $S = 0.847 \text{ GeV}^{1/2}$, and the constant term is $C = 0.074$
 296 [4].

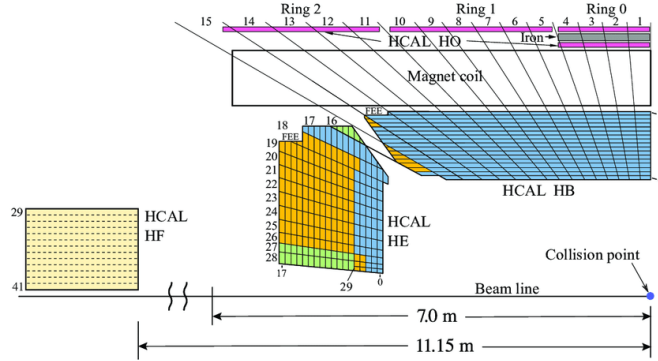


Fig. 4.7: Longitudinal view of HCAL [2]

297 4.6 Superconducting Solenoid

298 In between the HCAL barrel and outer barrel is the superconducting solenoid
 299 magnet. The magnet is 12 m long with a 6-m inner diameter and provides
 300 the bending power necessary to precisely measure the momentum of charged
 301 particles. While it is capable of producing a 4 T magnetic field, the magnet
 302 is typically operated at 3.8 T. This is done to prolong the lifetime of the
 303 magnet. The Niobium Titanium coils used to create the uniform 3.8-T
 304 magnetic field are suspended in a vacuum cryostat and cooled by liquid helium
 305 to a temperature of 4.5 K. The magnet has a stored energy of 2.6 GJ when
 306 operating at full current. There are five wheels in the barrel and three
 307 disks on each endcap that make up a 12,000 ton steel yoke which serves to
 308 return the magnetic flux. This, along with a mapping of the calculated field
 309 strength, can be seen in Figure 4.8. More details on the superconducting
 310 solenoid magnet can be found at [1]

311 4.7 Muon System

312 Embedded in magnet return yoke and encapsulating all of the other sub-
 313 detectors is the muon system. The muon system is the outermost layer
 314 because muons don't interact via the strong force and electromagnetic in-
 315 teractions alone are not enough to stop them due to their large mass, therefore
 316 the only particles that are capable of making it to the muon system are
 317 muons and weakly-interacting particles such as neutrinos. The muon sys-
 318 tem is comprised of three different types of detectors. These are drift tube
 319 (DT) chambers, cathode strip chambers (CSC), and resistive plate chambers

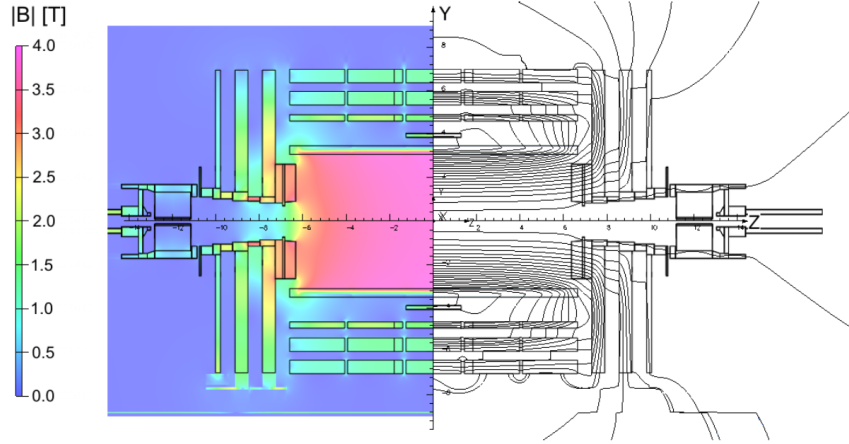


Fig. 4.8: Longitudinal slice of CMS detector while operating at 3.8-T central magnetic field. The right-hand side of the figure shows a mapping of the magnetic field lines while the left-hand side shows a mapping of the field strength. Reprint from [10]

320 (RPC). A cross-sectional view of the muon system along with the rest of the
 321 CMS detector is shown in Figure 4.9.

322 The DT chambers are used barrel region for $|\eta| < 1.2$. Each chamber is
 323 comprised of three superlayers which are made up of four staggered layers
 324 of rectangular drift cells. Each of these drift cells contains a mixture of
 325 Ar and CO₂ gases. An anode wire, located at the center of each tube, is
 326 made of gold-plated stainless steel and is held at 3.6 kV. The gas is ionized
 327 when a charged particle passes through and the resulting free electrons are
 328 attracted to the anode wire. As these electrons pass through the gas they
 329 cause further ionization which results in an electron avalanche. The layers
 330 of drift cells are oriented in such a way that two of the three superlayers
 331 give the muon position in the ϕ -direction and one gives the position in the
 332 z -direction. The result is a spacial resolution of 77-123 μm along the ϕ
 333 direction and 133-193 μm along the z direction for each DT chamber [14].

334 On the endcaps, covering the pseudorapidity range of $0.9 < |\eta| < 2.4$,
 335 are the CSCs. In this region there is a higher muon flux as well non-uniform
 336 magnetic fields so this portion of the muon system must have higher gran-
 337 ularity provided by the CSCs. Each of these chambers contain panels that
 338 divide it into six staggered layers. The cathode strips are oriented along the
 339 r -direction to give position measurements in the ϕ -direction while anode
 340 wires run perpendicular in between the panels to give r -direction position

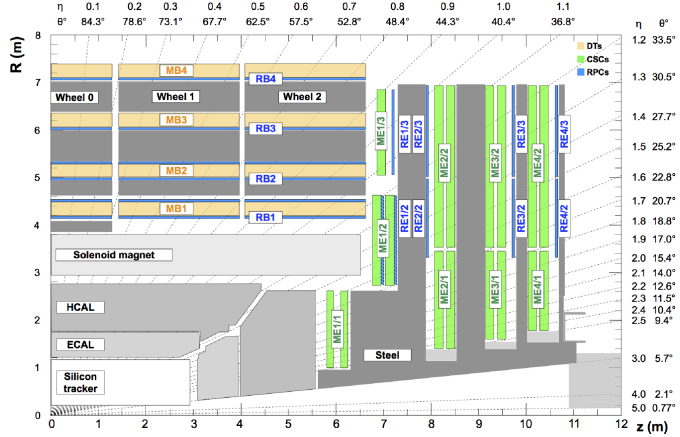


Fig. 4.9: Cross-section of one quadrant of the CMS detector. The DTs are labeled as "MB" (Muon Barrel) and the CSCs are labelled as "ME" (Muon Endcap). The RPCs are "RB" for those in the barrel and "RE" for those in the endcap. Reprint from [20].

341 measurements. The spacial resolution provided by the CSCs is 45-143 μ m
 342 [20].

343 Both the endcap and barrel regions, spanning $|\eta| < 1.6$, contain RPCs to
 344 provide more precise timing measurements. Each RPC is a gaseous parallel-
 345 plate detector. High voltage is applied to two large plates which have a
 346 layer of gas between them. Outside the chamber is an array of cathode
 347 strips which is used to detect electron cascades resulting from muons passing
 348 through and ionizing the gas. Where the DTs and CSCs provide precise
 349 position information, the RPCs have a very fast response time which gives
 350 a time resolution better than 3 ns [20]. This allows for the RPCs to be used
 351 as a dedicated muon trigger that can insure each muon is assigned to the
 352 correct bunch crossing.

353

5. MIP TIMING DETECTOR (MTD)

354

5.1 Introduction

355 In the coming years the LHC will be working toward upgrades that will
 356 lead a substantial increase in luminosity. The timeline for future operations
 357 of the LHC is shown in Figure 5.1. In 2019 the LHC entered a two-year
 358 shutdown, Long Shutdown 2 (LS2). Upgrades of the LHC injector complex
 359 to increase the beam brightness will take place during this shutdown. After
 360 LS2 the LHC will enter Run 3 which will run for three years at 13-14 TeV. At
 361 the completion of Run 3 the LHC will enter Long Shutdown 3 (LS3) which
 362 will last approximately 2.5 years. During LS3 the optics in the interaction
 363 region will be upgraded to produce smaller beams at the interaction point.
 364 The completion of this upgrade will usher in the High Luminosity (HL-LHC)
 365 era or Phase 2 of LHC operations, during which the combination of brighter
 366 beams and a new focusing scheme at the IP allows for a potential luminosity
 367 of $2 \times 10^{35} \text{ cm}^{-2}\text{s}^{-1}$ at the beginning of each fill [5].

LHC/ High-Luminosity LHC timeline

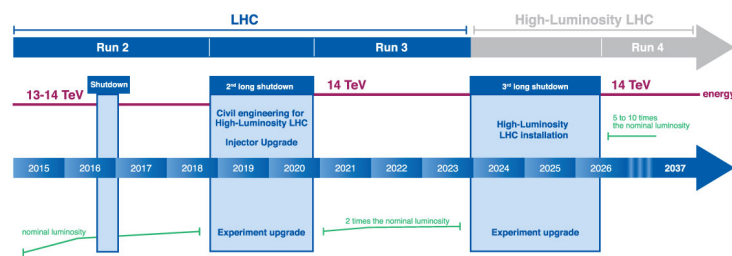


Fig. 5.1: Timeline for LHC [15]

368

The increased luminosity results in more interactions per bunch crossing or pileup. In order to limit the amount of pileup the experiments must

disentangle to more manageable levels, the nominal scenario would be operating at a stable luminosity of $5.0 \times 10^{34} \text{ cm}^{-2} \text{ s}^{-1}$. This would limit the pileup to an average of 140. The ultimate scenario for operations would be running at $7.5 \times 10^{34} \text{ cm}^{-2} \text{ s}^{-1}$ which brings the average pileup up to 200. The CMS detector in its current state is not capable of dealing with $\approx 140\text{-}200$ pileup. At this level of pileup the spacial overlaps of tracks and energy depositions would lead to a degradation in the ability to identify and reconstruct hard interactions. In order to preserve the data quality of the current CMS detector this increased pileup must be reduced to an equivalent level approximately equal to current LHC operations which is ~ 40 . The collision vertices within a bunch crossing have an RMS spread of 180-200 ps in time. If the beam spot were to be sliced into consecutive snap shots of 30-40 ps then the pileup levels per snapshot would be approximately 40. The space-time reconstruction of a 200 pileup event is shown in Figure 5.2. The addition of timing information to the z position spreads apart the vertices that would otherwise have been merged together and indiscernible. In order to achieve this a detector dedicated to the precise timing of minimum ionizing particles (MIPs), the MTD, will be added to the CMS detector.

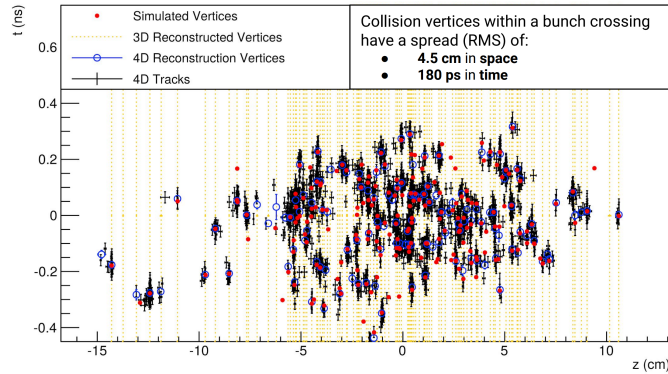


Fig. 5.2: Vertices from a simulated 200 pileup event. Need to replace this with the figure from the TDR.

388

5.2 Barrel Timing Layer

389 The Barrel Timing Layer (BTL) makes up the barrel region of the MTD.
 390 It will provide pseudorapidity coverage up to $|\eta| = 1.48$ with a geometric
 391 acceptance of $\sim 90\%$. The BTL will be capable of detecting MIPs with a
 392 time resolution of 30 ps at the start of Phase-2 operations and a luminosity-

³⁹³ weighted time resolution of ~ 45 ps when radiation damage effects are taken
³⁹⁴ into account.

6. CMS TRIGGER SYSTEM

396 When operating at nominal luminosity the LHC produces over 1 billion
 397 proton-proton collisions per second. Finite computing speed and storage
 398 capacity limit the rate at which CMS can record events to be about 1 kHz
 399 [8]. Decreasing the rate from 1 GHz to 1 kHz is accomplished by using a
 400 two-level trigger system to quickly decide which events will be discarded
 401 and which will be recorded. The first stage is a hardware-based Level 1 (L1)
 402 trigger and the second stage is software-based High Level Trigger (HLT).

6.1 *L1 trigger*

404 The L1 trigger decreases the rate by about six orders of magnitude from 1
 405 GHz to 100 kHz by performing rough calculations on information from the
 406 ECAL, HCAL, and muon subsystems using field-programmable gate arrays
 407 (FPGAs). The L1 trigger can be divided further into the calorimeter and
 408 muon triggers. The schematic of the L1 trigger system in Figure 6.1 shows
 409 both the calorimeter and muon triggers. The calorimeter trigger trigger
 410 uses information from the ECAL and HCAL subdetectors to construct pho-
 411 ton, electron, and jet candidates in addition to quantities such as missing
 412 transverse momentum and total hadronic activity. The muon trigger uses
 413 information from all three muon subsystems to construct muon candidates.
 414 The outputs from the calorimeter and muon triggers goes into the Global
 415 Trigger (GT) which decides which events should be recorded and which are
 416 to be discarded [21].

6.1.1 *Calorimeter trigger*

418 Trigger Primitives (TP) are the raw inputs from the ECAL and HCAL
 419 for the calorimeter trigger. The TP, which contain information regarding
 420 the energy deposits in the calorimeters, are passed to the first layer of the
 421 calorimeter trigger. This first layer consists of several FPGA cards that
 422 receive data from several bunch crossings, but are each mapped to a section
 423 of the detector. This data is then passed on to the second layer in such a way

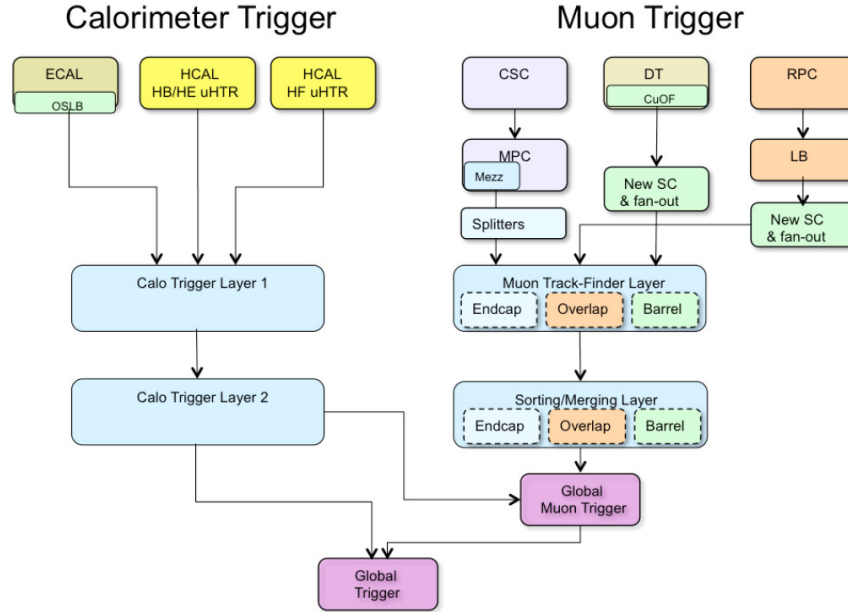


Fig. 6.1: L1 trigger system. Reprint from [3]

424 that each FPGA in this layer will receive data for the entire calorimeter for
 425 each bunch crossing. Candidate objects are then constructed and organized
 426 into a sorted list according to transverse momentum and passed on to the
 427 GT and the global muon trigger.

428 6.1.2 Muon trigger

429 TP for the muon trigger come from the three muon detectors, the CSCs,
 430 DTs, and RPCs. These are then passed on to the first layer of the muon
 431 trigger (Muon Track-Finding Layer) where the TP are combined to recon-
 432 struct muon tracks for sections of ϕ for different regions of $|\eta|$. The barrel
 433 track-finder for $|\eta| < 0.83$, the endcap track-finder for $|\eta| > 1.24$, and the
 434 overlap track-finder for $0.83 < |\eta| < 1.24$. This data is passed on to the
 435 second layer where the sections of ϕ are merged and subsequently passed
 436 on to the global muon trigger where it is combined with the output from
 437 Calo Trigger Layer 2 to compute isolation. The global muon trigger then
 438 combines the η regions and passes a list of the top eight muon candidates
 439 to the GT.

 440 *6.1.3 Global Trigger*

441 Final processing of the reconstructed objects and quantities constructed by
 442 the calorimeter and muon triggers is carried out by the GT. L1 algorithms
 443 or "seeds" are implemented by the GT using these objects. A full set of L1
 444 seed is called a L1 menu and can be adjusted to meet the requirements of
 445 the CMS physics program. Each L1 seed can be given a "prescale", which is
 446 an integer value N that can be used to reduce the rate of a particular trigger
 447 path. This is done by only applying the trigger to one out of N events and
 448 can be used to take advantage of the current LHC running conditions.

 449 *6.2 High Level Trigger*

450 Events that are accepted by the L1 trigger are passed on to the HLT which
 451 is based in software and is therefore capable of analyzing events with a higher
 452 degree of sophistication. The HLT has access to information from the full
 453 detector and implements "paths" to select events of interest from those pass-
 454 ing the L1 trigger. Each HLT path is a set of criteria that is used to either
 455 accept or reject an event. The full set of HLT paths is the HLT menu. Each
 456 HLT path is "seeded" by one or more L1 seeds in order to decrease comput-
 457 ing time. That means that a given HLT path will only be processed if the
 458 L1 bits associated with its seed or seeds fire. Each HLT path is assigned to
 459 a primary dataset depending on its general physics signature. In the case
 460 of this analysis, the primary dataset used for signal events was DoubleEG
 461 for years 2016 and 2017. This was merged into the EGamma dataset for
 462 2018. The SingleMuon dataset was used for trigger efficiency studies. A list
 463 of the primary HLT used for each year along with its associated primary
 464 dataset is listed in Table 6.1. The HLT path for 2016 is different because
 465 HLT_DoublePhoton70 was not a part of the HLT menu until 2017.

Tab. 6.1: Primary HLT

| Year | HLT path | Primary dataset |
|------|--------------------|-----------------|
| 2016 | HLT_DoublePhoton60 | DoubleEG |
| 2017 | HLT_DoublePhoton70 | DoubleEG |
| 2018 | HLT_DoublePhoton70 | EGamma |

 466 *6.3 Trigger efficiency*

467 7. CMS PARTICLE AND EVENT RECONSTRUCTION

468 After an event is chosen to be stored by the trigger system, the output from
469 all of the sub-detectors is saved and recorded to disk as "RAW" data. These
470 data contain information about the response of each sub-detector, such as
471 tracker hits and energy deposition in the calorimeters. As was mentioned
472 in Chapter 4, shown in Table 4.1 and Figure 4.2, the CMS was designed
473 such that each type of particle resulting from the pp collisions at the IP
474 would leave a distinct signature in the sub-detectors. This allows for the
475 information to be reconstructed into lists of physics object candidates such
476 as photons, electrons, muons, etc and quantities such as missing transverse
477 momentum. The particle flow (PF) algorithm performs this reconstruction
478 by first building tracks and calorimeter clusters. These two elements are the
479 inputs to the reconstruction of the aforementioned physics object candidates
480 using a "link" algorithm.

481 7.1 *Tracks*

482 A combinatorial track finder algorithm based on the Kalman filtering tech-
483 nique uses the hits in the silicon tracker to reconstruct tracks of charged
484 particles [17]. Each iteration of the algorithm is comprised of three steps:

- 485 • Seed generation: Find a seed consisting of two to three hits that is
486 compatible with a track from a charged particle.
- 487 • Track finding: Use pattern recognition to identify any hits that are
488 compatible with the trajectory implied by the seed generated in the
489 first step.
- 490 • Track fitting: Determine the properties of the track, such as origin,
491 trajectory, and transverse momentum by performing a global χ^2 fit.

492 The first iteration uses stringent requirements on the seeds and the χ^2
493 of the track fit to pick out isolated jets which have very high purity. The
494 hits associated with these high purity tracks are then removed to reduce the

495 combinatorial complexity for subsequent iterations. This allows successive
496 iterations to identify less obvious tracks by progressively loosening criteria
497 while the removal of previously associated hits mitigates the likelihood of
498 fake tracks being built.

499 **7.2 Calorimeter clusters**

500 Calorimeter clusters are constructed using energy deposition information
501 from the calorimeters. Clusters are formed by first identifying the seed cell
502 (ECAL crystal or HCAL scintillating tile) that corresponds to the local
503 maxima of an energy deposit that is above a given threshold. Neighboring
504 cells are then aggregated to grow topological clusters if their signals are
505 above twice the standard deviation of the level of electronic noise.

506 **7.3 Object identification**

507 At this point the tracks and calorimeter clusters are linked to form a PF
508 block. This linkage is done with an algorithm that quantifies the likelihood
509 that a given track and cluster were results of the same particle. As PF blocks
510 are identified as object candidates they are removed from the collection prior
511 to each subsequent iteration until all tracks and clusters have been assigned
512 to a PF object candidate. The following sections will outline how each of
513 these PF objects is identified.

514 **7.3.1 Muons**

515 Muons are the easiest particle to identify, so they are the first objects recon-
516 structed in the CMS. PF Muons are classified in three categories depending
517 on how their tracks are reconstructed:

- 518 • Tracker muons: Tracks reconstructed from the inner tracker having
519 $p_T > 0.5$ GeV and $|\vec{p}| > 2.5$ GeV that, when propagated to the muon
520 system, match at least one hit in the muon chambers.
- 521 • Stand-alone muons: Tracks reconstructed only using hits in the muon
522 system.
- 523 • Global muons: Stand-alone muons that coincide with a track from the
524 inner tracker.

525 After a muon is reconstructed it is given an identification or ID based on
526 observables such as the χ^2 of the track fit, how many hits were recorded

527 per track, or how well the tracker and stand-alone tracks matched. These
528 IDs represent different working points (loose, medium, and tight) which
529 correspond to increasing purity but decreasing efficiency as you move from
530 loose toward tight.

531 **7.3.2 Electrons**

532 The next objects reconstructed in the CMS are electrons. Bremsstrahlung in
533 the tracker layers causes substantial energy loss and changes in momentum
534 which requires the use of a dedicated tracking algorithm. In place of the
535 Kalman filtering technique, a Gaussian-sum filter (GSF) algorithm is used.
536 This algorithm uses a weighted sum of Gaussian PDFs which does a bet-
537 ter job of modeling the Bremsstrahlung effects than the Kalman filtering
538 technique which uses a single Gaussian PDF.

539 PF ECAL clusters are regrouped by identifying a seed cluster then asso-
540 ciating and adding clusters from Bremsstrahlung photons to form superclus-
541 ters. The schematic in Figure 7.1 shows how the Bremsstrahlung photons
542 are emitted in directions tangent to the trajectory of the electron. Electrons
543 bending in the magnetic field causes spreading of PF ECAL clusters to typ-
544 ically occur along the ϕ -direction. Two approaches are used to associate
545 the superclusters to GSF tracks. One is the ECAL-driven method, which
546 uses superclusters with $p_T > 4$ GeV as seeds for the GSF track finding al-
547 gorithm. This works well for high- p_T isolated electrons because the bend
548 radius is less severe which decreases the spread of the PF ECAL clusters.
549 This results in more of the Bremsstrahlung radiation being recovered and
550 correctly associated with an electron candidate. The second approach is the
551 tracker-driven method which uses tracks with $p_T > 2$ GeV as seeds that are
552 propagated out to the surface of the ECAL and used for clustering. This
553 method works best with soft electrons like those in jets because it relies on
554 the high granularity of the tracker to disentangle overlapping energy deposits
555 in the ECAL. [18]

556 As a final step, a boosted decision tree (BDT) is used to discriminate
557 between real and fake electrons. The BDT is given variables associated with
558 track-cluster matching, shower shape, and tracking. The output score of
559 the BDT is used to classify electrons into loose, medium, and tight working
560 points which exhibit the same purity and efficiency trends as the muon
561 working points.

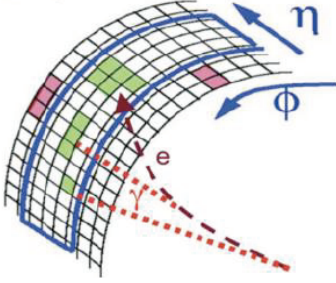


Fig. 7.1: The Bremsstrahlung photons continue along a straight trajectory while the electron path is bent by the magnetic field. This results in energy deposited in the calorimeter for such electrons to be spread out along the ϕ -direction.

562

7.3.3 Photons

563 Unlike electrons, photons typically deposit most of their energy in the ECAL
 564 without interacting with the tracker therefore their reconstruction is seeded
 565 from ECAL superclusters that do not have any GSF tracks associated with
 566 them. When photons interact with the tracker material they convert into
 567 electron-positron pairs which follow bent trajectories due to the magnetic
 568 field prior to entering the ECAL. This causes a spread of the energy deposi-
 569 tion along the ϕ -direction. The goal of the clustering algorithm for photon
 570 reconstruction is to include all of the energy deposits of electrons resulting
 571 from photon conversions. As with the calorimeter clustering algorithm, the
 572 photon clustering starts by identifying a local energy maxima as a seed crys-
 573 tal. In the EB a cluster is made up of several parallel strips of crystals 5×1
 574 in $\eta \times \phi$. The first strip has the seed crystal at its center. Neighboring strips
 575 in the ϕ -direction are added if they have energy above a threshold of 10 GeV
 576 but less than that of the subsequent strip with a maximum of 17 strips in
 577 a cluster. In the EE, the seed cluster is 5×5 with adjacent 5×5 clusters
 578 being added if they meet the minimum energy requirement.

579 Converted and unconverted photons can be differentiated by looking at
 580 how the energy is distributed in a supercluster. The variable R_9 is used for
 581 this purpose. It is defined as the ratio of the energy in a 3×3 crystal array to
 582 the energy in the entire supercluster. As the energy deposits resulting from
 583 converted electrons is more spread out they result in a lower R_9 value than
 584 unconverted photons. A photon is candidate is considered to be unconverted
 585 when $R_9 > 0.93$.

586 An important point regarding the clustering algorithm is that it does
 587 not differentiate between showers resulting from photons and those resulting
 588 from electrons. This allows for electron from $Z \rightarrow ee$ events to be used as
 589 high purity samples to study analysis inputs and for defining control regions
 590 using electron in place of photons.

591 7.3.4 Jets

592 When quarks or gluons are produced they hadronize to make cone-shaped,
 593 collimated collections of particles called jets. The jet clustering algorithm
 594 aims to combine these particles in order to accurately measure the kine-
 595 matics of the initial gluon or quark. The algorithm uses the two distance
 596 parameters

$$d_{ij} = \min(k_{T_i}^{2p}, k_{T_j}^{2p}) \frac{\Delta R_{ij}^2}{R^2} \quad (7.1)$$

$$d_{iB} = k_{T_i}^{2p} \quad (7.2)$$

597 where d_{ij} is the distance between objects i and j and d_{iB} is the distance
 598 between object i and the beam B . The transverse momentum of the object is
 599 k_T . The parameter p is set either -1, 0, or +1 to specify whether the anti- k_T ,
 600 inclusive Cambridge/Aachen, or inclusive k_T algorithm is used, respectively.
 601 The value of ΔR_{ij}^2 is defined as $(\eta_i - \eta_j)^2 + (\phi_i - \phi_j)^2$ and R is the distance
 602 parameter that defines the radius of the jet.

603 his analysis uses jets reconstructed from PF candidates using the anti- k_T
 604 algorithm with $R = 0.4$, also known as AK4PFJets or just PFJets. The
 605 algorithm goes through the following steps:

- 606 1. The smallest values of d_{ij} and d_{iB} are computed for all objects in the
 607 event.
- 608 2. Objects i and j are merged into a single object if $d_{ij} < d_{iB}$.
- 609 3. Object i is labeled as a jet and removed from the list if $d_{iB} < d_{ij}$.

610 Note for next time: Now talk about infrared and collinear safe. Use
 611 Allie's thesis for guide. Look at "recent thesis" for ECAL noise on 2017
 612 data. Should also do JEC and JER in here.

613 7.4 Missing transverse momentum

614

8. DATA ANALYSIS

615

8.1 Overview

616 This analysis is motivated by the GGM supersymmetry breaking scenario
 617 in which the strong production of either gluinos or squarks result in a final
 618 state containing two photons, jets, and missing transverse momentum. Two
 619 example topologies are shown in Figure 8.1. If the T5gg model, each of the
 620 produced gluinos decays to a neutralino which then decays to a photon and
 621 a gravitino. Similarly, the T6gg model has each of the produced squarks
 622 decays to a neutralino which then decays to a photon and a gravitino. In
 623 both cases the gravitino escapes the CMS without detection which manifests
 624 as missing transverse momentum.

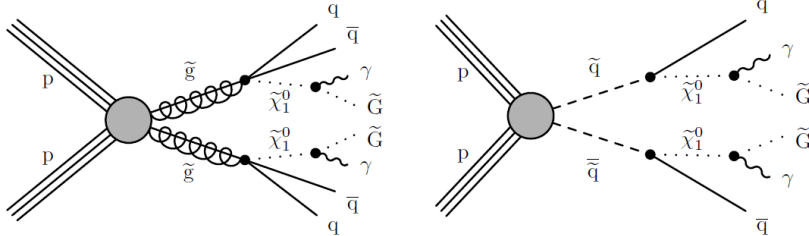


Fig. 8.1: Two examples of GGM supersymmetry breaking processes resulting in final states containing two photons and missing transverse momentum. The T5gg model (left) shows gluinos produced from $p - p$ collisions which subsequently result in two neutralinos, each decaying to a photon and a gravitino. The T6gg model (right) shows squarks produced from $p - p$ collisions following a similar decay chain.

625

8.2 Data

626 This analysis was performed using 137 fb^{-1} of data collected from the CMS
 627 detector during the time period commonly referred to as Run 2 which spans
 628 from 2016 to 2018. The complete list of the datasets used can be found in

629 Table 8.1. The JSON files used to identify events passing all of the CMS
 630 offline data quality monitoring requirements are:

631 Cert_271036_284044_13TeV_23Sep2016ReReco_Collisions16_JSON.txt
 632 Cert_294927_306462_13TeV_EOY2017ReReco_Collisions17_JSON_v1.txt
 633 Cert_314472_325175_13TeV_PromptReco_Collisions18_JSON.txt

Tab. 8.1: Data Samples

| |
|---------------------------------------|
| /DoubleEG/Run2016B-17July2018-ver2-v1 |
| /DoubleEG/Run2016C-17July2018-v1 |
| /DoubleEG/Run2016D-17July2018-v1 |
| /DoubleEG/Run2016E-17July2018-v1 |
| /DoubleEG/Run2016F-17July2018-v1 |
| /DoubleEG/Run2016G-17July2018-v1 |
| /DoubleEG/Run2016H-17July2018-v1 |
| /DoubleEG/Run2017B-31Mar2018-v1 |
| /DoubleEG/Run2017C-31Mar2018-v1 |
| /DoubleEG/Run2017D-31Mar2018-v1 |
| /DoubleEG/Run2017E-31Mar2018-v1 |
| /DoubleEG/Run2017F-31Mar2018-v1 |
| /EGamma/Run2018A-17Sep2018-v2 |
| /EGamma/Run2018B-17Sep2018-v1 |
| /EGamma/Run2018C-17Sep2018-v1 |

634 8.3 Monte Carlo samples

635 Monte Carlo (MC) simulation were used to validate performance of the
 636 analysis on backgrounds, model background contributions, constructing a
 637 multivariate discriminant, and determining signal efficiencies.

638 8.4 Object definitions

639 The object candidates that are identified by the reconstruction algorithms
 640 are subject to further scrutiny in order to achieve optimal purities in the
 641 offline analysis.

 642 **8.4.1 Photons**

643 Photons are required to have $p_T > 75$ GeV and meet the criteria prescribed
 644 by loose ID cuts derived by the e/γ Physics Object Group (EGM POG).
 645 The cut variables used to determine the photon ID are:

- 646 • H/E - The ratio of the energy deposited in the HCAL tower that is
 647 directly behind the ECAL supercluster associated with the photon to
 648 the energy deposited in the ECAL supercluster.
- 649 • $\sigma_{i\eta i\eta}$ - The log-fractional weighted width of a shower in $i\eta$ -space. This
 650 variable is used to describe the shower shape.
- 651 • Particle Flow Charged Isolation - Sum of the p_T of charged hadrons
 652 associated with the primary vertex within a cone of $0.02 < \Delta R < 0.3$
 653 of the supercluster.
- 654 • Particle Flow Neutral Isolation - Sum of the p_T of neutral hadrons
 655 associated with the primary vertex within a cone of $\Delta R < 0.3$ of the
 656 supercluster.
- 657 • Particle Flow Photon Isolation - Sum of the p_T of photons within a
 658 cone of $\Delta R < 0.3$ of the supercluster.

659 All of the isolation variables listed above are corrected in order to remove
 660 pileup. Table 8.2 gives a summary of the pileup-corrected requirements for a
 661 loose ID photon. The loose ID working point has an efficiency (background
 662 rejection) of 90.08% (86.25%) in the barrel and 90.65% (76.72%) in the end
 663 caps. In addition to the p_T and loose ID requirements, a photon must also
 664 pass a pixel seed veto (PSV). This means that there is no pixel seed matched
 665 to the photon.

Tab. 8.2: Summary of loose ID photons cuts

| Variable | Cut Value (Barrel) | Cut Value (Endcap) |
|------------------------|---|--|
| H/E | 0.04596 | 0.0590 |
| $\sigma_{i\eta i\eta}$ | 0.0106 | 0.0272 |
| Charged Iso | 1.694 | 2.089 |
| Neutral Iso | $24.032 + 0.01512 p_{T\gamma} + 2.259 \times 10^{-5} p_{T\gamma}^2$ | $19.722 + 0.0117 p_{T\gamma} + 2.3 \times 10^{-5} p_{T\gamma}^2$ |
| Photon Iso | $2.876 + 0.004017 p_{T\gamma}$ | $4.162 + 0.0037 p_{T\gamma}$ |

666

8.4.2 Electrons

667 As mentioned earlier, the clustering algorithm doesn't differentiate between
668 showers from photons and those from electrons. In this analysis an electron
669 is defined as an object that passes all of the photon requirements except
670 for the PSV. Inverting the pixel seed requirement while using the same
671 ID criteria insures that we have orthogonal selections while minimizing the
672 bias potentially introduced by using control regions with electrons to model
673 diphoton signal regions.

674

8.4.3 Muons

675

8.5 Backgrounds

676 The sources of background in this analysis can be grouped into three cate-
677 gories. In order of decreasing contribution they are mismeasured hadronic
678 activity, electrons misidentified as photons, and standard model processes
679 having final states with neutrinos and two photons. In events with mul-
680 tiple jets, limitations on the jet energy resolution can give rise to an ap-
681 parent imbalance in p_T as is shown in Figure 8.2. Such events are usually
682 from quantum chromodynamics (QCD) processes. In these cases jets can
683 be misidentified as photons or there can be real photons being produced.
684 In both cases the result is the appearance of two photons accompanied by
685 E_T^{miss} which mimics our signal. Given the large cross-section for QCD, this
686 is the most significant background in this analysis. The next background,
687 resulting from the misidentification of electrons as photons, comes from elec-
688 troweak (EWK) processes, in particular $W\gamma$ and $W + \text{jets}$ events where
689 $W \rightarrow e\nu$. Here the neutrino contributes real E_T^{miss} while the fake photon
690 allows this event to fulfill the diphoton requirement. The final background
691 is from $Z\gamma\gamma \rightarrow \nu\nu\gamma\gamma$ events, which exactly mimic our signal, and is modeled
692 using simulation as it is irreducible.

693

8.5.1 Instrumental background

694 The instrumental background is the contribution from events with spurious
695 E_T^{miss} due to mismeasured hadronic activity. Since most of this background
696 is comprised of QCD events, it is commonly referred to as the "QCD back-
697 ground" and those terms are used interchangeably in this thesis. Modeling of
698 this background was done using the Rebalance and Smear technique while
699 a multivariate discriminant was constructed to improve the efficiency of
700 identifying events with fake E_T^{miss} .

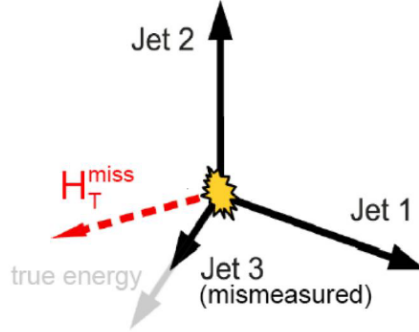


Fig. 8.2: Mismeasurement of Jet3 results in an imbalance in the events transverse momentum.

701 *Rebalance and smear*

702 The rebalance and smear method is used to estimate the QCD background
703 by

704 *Multivariate discriminant*

705 *8.5.2 Electroweak background*

706 Need to look at this again

707 The electroweak background is dominated by events with $W \rightarrow e\nu$ where
708 the electron is misidentified as a photon. Unlike the QCD background these
709 events have real E_T^{miss} due to the presence of a neutrino. The key to estimat-
710 ing this background is determining the rate at which electrons get incorrectly
711 labeled as photons in the signal region. This is done using a tag-and-probe
712 method where the tag is an electron (a loose ID photon that fails the PSV)
713 and the probe is categorized as either a photon or an electron. The result
714 is an electron-electron region (ee) and an electron-photon region ($e\gamma$) that
715 are selected from the data. As both of these regions contain $Z \rightarrow ee$ decays,
716 fits are applied in each of the samples to the invariant mass spectra m_{ee} and
717 $m_{e\gamma}$. The integrals of these fits are calculated over the range of the Z mass
718 peak to give

719 This is done using two control regions. The first is double electron (ee)
720 region. As described before, the electrons are defined as loose ID photons
721 that have a pixel seed match. The second is the $e\gamma$ region which contains
722 one electron and one photon. The misidentification rate can be calculated
723 by comparing the invariant mass peaks m_{ee} and $m_{e\gamma}$.

724 *8.5.3 Irreducible background*

725 The irreducible $Z\gamma\gamma \rightarrow \nu\nu\gamma\gamma$ background produces two photons and has
726 inherent E_T^{miss} via the neutrinos. There is no easy way to separate these
727 events from our signal so it is estimated using MC simulation. The modeling
728 of this background was tested using $Z\gamma\gamma \rightarrow \mu\mu\gamma\gamma$ events in data. Dimuon
729 events with $|m_{\mu\mu} - m_Z| < 10$ GeV were selected and the contribution of the
730 muons was removed from the E_T^{miss} calculation to mimic $Z \rightarrow \nu\nu$.

BIBLIOGRAPHY

- [1] *The CMS electromagnetic calorimeter project: Technical Design Report.* Technical design report. CMS. CERN, Geneva, 1997.
- [2] *The CMS hadron calorimeter project: Technical Design Report.* Technical design report. CMS. CERN, Geneva, 1997.
- [3] CMS Technical Design Report for the Level-1 Trigger Upgrade. 6 2013.
- [4] S. Abdullin et al. The CMS barrel calorimeter response to particle beams from 2-GeV/c to 350-GeV/c. *Eur. Phys. J. C*, 60:359–373, 2009. [Erratum: Eur.Phys.J.C 61, 353–356 (2009)].
- [5] G. Apollinari, O. Brüning, T. Nakamoto, and Lucio Rossi. High Luminosity Large Hadron Collider HL-LHC. *CERN Yellow Rep.*, (5):1–19, 2015.
- [6] S Baird. Accelerators for pedestrians; rev. version. Technical Report AB-Note-2007-014. CERN-AB-Note-2007-014. PS-OP-Note-95-17-Rev-2. CERN-PS-OP-Note-95-17-Rev-2, CERN, Geneva, Feb 2007.
- [7] David Barney. CMS Slice. Feb 2015.
- [8] L. Cadamuro. The CMS Level-1 trigger system for LHC Run II. *JINST*, 12(03):C03021, 2017.
- [9] Jean-Luc Caron. Cross section of lhc dipole.. dipole lhc: coupe transversale. ”AC Collection. Legacy of AC. Pictures from 1992 to 2002.”, May 1998.
- [10] S Chatrchyan et al. Precise Mapping of the Magnetic Field in the CMS Barrel Yoke using Cosmic Rays. *JINST*, 5:T03021, 2010.
- [11] CMS Collaboration. CMS Technical Design Report for the Pixel Detector Upgrade. Technical Report CERN-LHCC-2012-016. CMS-TDR-11, Sep 2012. Additional contacts: Jeffrey Spalding, Fermilab, Jef-

- frey.Spalding@cern.ch Didier Contardo, Universite Claude Bernard-Lyon I, didier.claude.contardo@cern.ch.
- [12] CMS Collaboration. Description and performance of track and primary-vertex reconstruction with the CMS tracker. *JINST*, 9(CMS-TRK-11-001. CERN-PH-EP-2014-070. CMS-TRK-11-001):P10009. 80 p, May 2014. Comments: Replaced with published version. Added journal reference and DOI.
 - [13] The CMS Collaboration. The CMS experiment at the CERN LHC. *Journal of Instrumentation*, 3(08):S08004–S08004, aug 2008.
 - [14] The CMS collaboration. The performance of the CMS muon detector in proton-proton collisions at $\sqrt{s}=7$ TeV at the LHC. *Journal of Instrumentation*, 8(11):P11002–P11002, nov 2013.
 - [15] Cinzia De Melis. Timeline for the LHC and High-Luminosity LHC. Frise chronologique du LHC et du LHC haute luminosité. Oct 2015. General Photo.
 - [16] Lyndon Evans and Philip Bryant. LHC machine. *Journal of Instrumentation*, 3(08):S08001–S08001, aug 2008.
 - [17] R. Fruhwirth. Application of Kalman filtering to track and vertex fitting. *Nucl. Instrum. Meth. A*, 262:444–450, 1987.
 - [18] Jonas Rembser. CMS Electron and Photon Performance at 13 TeV. *J. Phys.: Conf. Ser.*, 1162(1):012008. 8 p, 2019.
 - [19] Tai Sakuma and Thomas McCauley. Detector and event visualization with SketchUp at the CMS experiment. *Journal of Physics: Conference Series*, 513(2):022032, jun 2014.
 - [20] A.M. Sirunyan et al. Performance of the CMS muon detector and muon reconstruction with proton-proton collisions at $\sqrt{s}=13$ TeV. *Journal of Instrumentation*, 13(06):P06015–P06015, jun 2018.
 - [21] J. Wittmann, B. Arnold, H. Bergauer, M. Jeitler, T. Matsushita, D. Rabady, B. Rahbaran, and C.-E. Wulz. The upgrade of the CMS global trigger. *Journal of Instrumentation*, 11(02):C02029–C02029, feb 2016.